

Wrinkles, Ridges, Miura-Ori, and Moiré Patterns in MoSe₂ Using Neural Networks

Anikeya Aditya, Ankit Mishra, Nitish Baradwaj, Ken-ichi Nomura, Aiichiro Nakano, Priya Vashishta, and Rajiv K. Kalia*



Cite This: *J. Phys. Chem. Lett.* 2023, 14, 1732–1739



Read Online

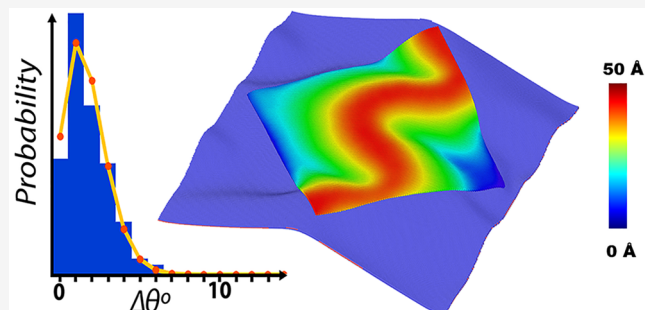
ACCESS |

Metrics & More

Article Recommendations

Supporting Information

ABSTRACT: Effects of lateral compression on out-of-plane deformation of two-dimensional MoSe₂ layers are investigated. A MoSe₂ monolayer develops periodic wrinkles under uniaxial compression and Miura-Ori patterns under biaxial compression. When a flat MoSe₂ monolayer is placed on top of a wrinkled MoSe₂ layer, the van der Waals (vdW) interaction transforms wrinkles into ridges and generates mixed 2H and 1T phases and chain-like defects. Under a biaxial strain, the vdW interaction induces regions of Miura-Ori patterns in bilayers. Strained systems analyzed using a convolutional neural network show that the compressed system consists of semiconducting 2H and metallic 1T phases. The energetics, mechanical response, defect structure, and dynamics are analyzed as bilayers undergo wrinkle–ridge transformations under uniaxial compression and moiré transformations under biaxial compression. Our results indicate that in-plane compression can induce self-assembly of out-of-plane metasurfaces with controllable semiconducting and metallic phases and moiré patterns with unique optoelectronic properties.



Downloaded via 68.181.17.163 on February 23, 2023 at 15:12:49 (UTC).
See https://pubs.acs.org/sharingguidelines for options on how to legitimately share published articles.

Graphene and two-dimensional (2D) transition metal dichalcogenides (TMDCs) display exceptional robustness and flexibility due to high in-plane and low out-of-plane stiffness.¹ The flexibility of 2D materials can be quantified by the Föppl–von Kármán number, which is proportional to the ratio of the in-plane Young's modulus to bending stiffness.² This number is extremely large for graphene and 2D TDMCs, and hence, they are as flexible as a sheet of paper.

The flexibility of 2D materials has been exploited to design kirigami and origami structures. Cai et al. have used chemical vapor deposition followed by chemical etching to design exotic kirigami structures of 2D WSe₂.³ Experiments, modeling and simulation, and machine learning have been used to design kirigami structures of graphene and 2D MoS₂ that are highly stretchable and recoverable upon loading and unloading.^{4,5} Two-dimensional materials can also be folded quite easily. Zhao et al. demonstrated this experimentally using directed fluid flow.⁵ They could control the folding geometry, direction, and position of 2D materials placed on polymer substrates in a microfluidic environment, and they were able to determine the underlying mechanism and energetics of folding using molecular dynamics (MD) simulations. Their joint experimental–simulation study has paved the way for the design of vertically stacked van der Waals (vdW) architectures in a microfluidic environment. These architectures exhibit a wide range of exotic phenomena such as superconductivity, atomic photonic crystals, topological excitons in stacked TMDCs,

magnetism, and Mott transition associated with moiré physics.^{6–18}

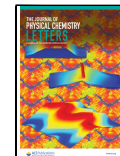
In this paper, we examine if ultrathin MoSe₂ sheets can form complex structures like wrinkles, ridges, and Miura-Ori patterns akin to those seen in nature during the opening and closing of leaves and wings of insects.^{19–21} Wrinkles were first observed in a thin metallic film on a polydimethylsiloxane substrate when the system was heated and then cooled to ambient temperature.²² It was argued that wrinkle formation was caused by compressive stress redistribution due to the buckling of stiff outer films, and it was shown that the dimensions of wrinkles could be controlled by the substrate structure.²¹ In subsequent experimental and simulation studies, period doubling of wrinkles and wrinkle-to-ridge transformation were seen in compressively strained thin films supported on soft substrates.^{19,21,23–28}

We have performed MD simulations to examine the effects of lateral compression on monolayer and bilayer MoSe₂.^{29–32} We use a convolutional neural network (CNN) trained on a prior MD data set of MoWSe₂ to demonstrate the viability of

Received: November 20, 2022

Accepted: January 19, 2023

Published: February 9, 2023



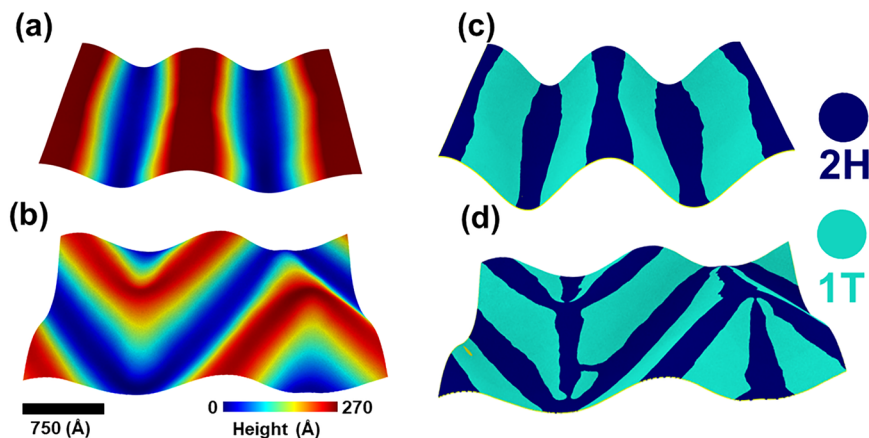


Figure 1. Effects of uniaxial and biaxial strains on a MoSe₂ monolayer. Here the applied strain is 6%, and the systems are at room temperature. Panels a and b show out-of-plane displacements in uniaxially and biaxially compressed systems, respectively. Peaks and valleys are colored red and blue, respectively. Periodic wrinkles are formed under uniaxial strain, and Miura-Ori patterns under biaxial strains. Inhomogeneous stress distributions induce structural transformations in strained monolayers. Stresses are small in magnitude in valleys and peaks, and hence, the structure remains in the 2H phase, although it is slightly strained (see panels c and d). Large stresses on the slopes of wrinkles and Miura folds induce 2H to 1T phase transformation under uniaxial and biaxial strains.

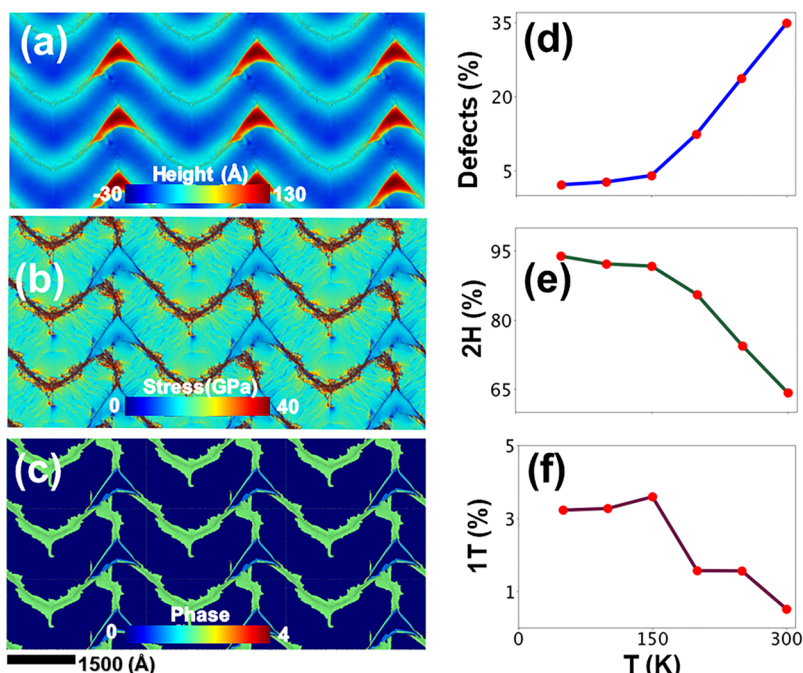


Figure 2. Effect of a biaxial strain (6%) on a MoSe₂ bilayer at room temperature. Out-of-plane displacements in panel a indicate the formation of a Miura-Ori pattern in the bilayer. Panel b shows inhomogeneous stresses in Miura folds, and panel c shows that the bilayer regions where the atomic-level stresses are relatively small remain in the 2H phase. There are small regions of high stress where the bilayer undergoes 2H to 1T phase transformation. Panel c also indicates point and line defects in high-stress regions (colored yellow and red in panel b). Panel d shows a linear increase in the number of defects, and panels e and f show linear decreases in the fractions of 2H and 1T phases with an increase in temperature above 150 K.

transfer learning in analyzing structural changes in strained monolayer and bilayer MoSe₂.^{33,34} We find that an unstrained MoSe₂ monolayer in the semiconducting 2H phase develops wrinkles under uniaxial compression and Miura-Ori patterns under biaxial compression. The wrinkled sheets are hybrid structures consisting of the 2H phase in low-stress regions around the peaks and valleys and the 1T phase in the high-stress slopy regions. Next, we study the effect of wrinkles and Miura folds on pristine overlayers of MoSe₂. When we place flat MoSe₂ monolayers above wrinkled MoSe₂ monolayers, the

bilayers bind by vdW interaction and wrinkles transform into ridges. The wrinkle–ridge transformation is accompanied by the appearance of mixed 2H and 1T phases and chain-like defects of Mo and Se atoms. In the case of biaxial strain, the vdW interaction induces a commensurate Miura-Ori pattern in the overlayer. The Miura-Ori patterns form novel moiré patterns under relative twisting of the two monolayers. The energetics, thermomechanical behavior, and defect dynamics are analyzed in MoSe₂ bilayers as they undergo wrinkle–ridge

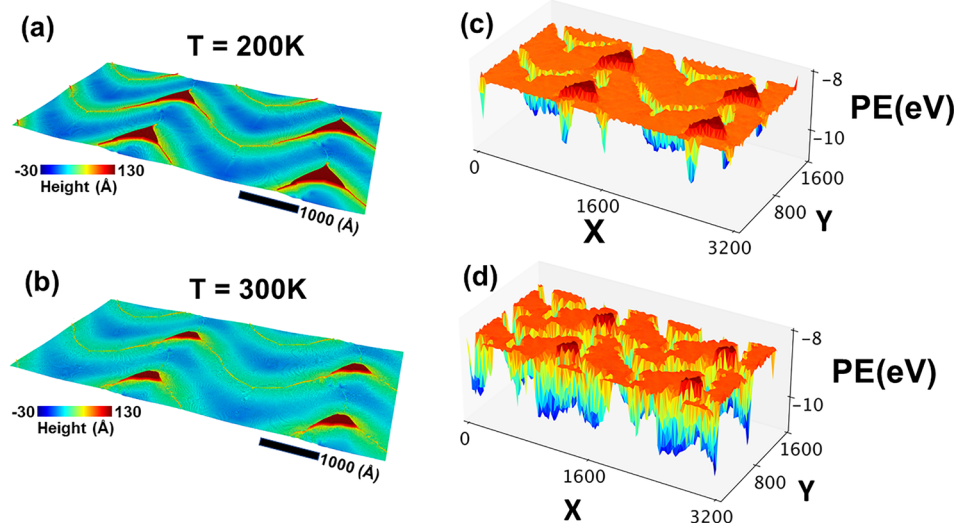


Figure 3. Potential energy surfaces (PES) underlying Miura-Ori patterns in a bilayer under a 6% biaxial compressive strain. Panels a and b show of out-of-plane displacements in the bilayer at temperatures of 200 and 300 K, respectively. The corresponding PES, which are the potential energies per particle averaged over all of the atoms in a pixel, are shown in panels c and d, respectively. In contrast to the out-of-plane atomic displacements, the PES show significant changes with an increase in temperature. The potential energy per pixel is high in regions of greater deformation.

transformations in uniaxially strained systems and moiré transformations of Miura folds in biaxially strained bilayers.

We have investigated the effect of vdW interaction on the formation of wrinkles, ridges, Miura folds, and moiré patterns in MoSe₂ bilayers. We simulated many bilayers with dimensions ranging from 400 Å × 200 Å to 3200 Å × 1600 Å. Here we present results for the largest system. Additional results are presented in the Supporting Information. We provide a video in the Supporting Information that shows the formation of wrinkles and Miura-Ori patterns and the emergence of 2H and 1T patterns. Figure 1 shows structural changes in MoSe₂ monolayers subjected to in-plane uniaxial and biaxial strains. In both cases, the compressive strain is 6% and the temperature is 300 K. Figure 1a shows out-of-plane atomic displacements in a uniaxially strained MoSe₂ monolayer. The displacements appear in the form of periodic wrinkles in the direction of compression (x). Blue regions represent valleys below the unstrained monolayer, and red regions indicate wrinkle peaks. The wrinkle amplitude is ~ 130 Å. The wrinkles result from inhomogeneous stress distributions, which are shown in Figure S3. Peaks and valleys have smaller stresses than the slopes of wrinkles. The CNN analysis of atomic configurations is presented in panels c and d of Figure 1. Under uniaxial compression, the monolayer becomes a hybrid structure of semiconducting (2H) and metallic (1T) phases that are colored blue and cyan, respectively. In Figure 1c, the 2H phase exists in small stress regions, i.e., peaks and valleys of wrinkles in which the top and bottom Se layers have shifted slightly relative to each other. Larger tensile stresses on the slopes of wrinkles induce a 2H → 1T phase transformation by changing the Se–Mo–Se stacking from ABA to ABC. At higher strains, we observe period doubling of wrinkles that has also been seen experimentally in thin films supported on soft substrates.¹⁹

Figure 1b shows that biaxial compression generates Miura-Ori patterns in the monolayer. The corresponding inhomogeneous stresses in the monolayer are shown in Figure S3. These stresses give rise to interesting patterns of 2H and 1T phases. The CNN analysis reveals the presence of the 1T phase along

with point and line defects in high-stress regions. The line defects are chains of 5- and 7-fold coordinated Mo atoms and 4-fold coordinated Se atoms. These defects, called α and β , were first seen in scanning transmission electron microscopy (STEM) images of MoS₂.³³

The vdW interaction induces significant structural changes in MoSe₂ bilayers. Wrinkles in a uniaxially strained monolayer disappear, and a ridge appears when the strained and pristine layers bind (see Figure S4). The ridges run straight across the bilayer in uniaxially compressed MoSe₂. Figure S5 shows that the ridge height increases with an increase in strain because atoms tend to move from high-stress to low-stress regions, i.e., to the top of ridges. Figure S6 shows that an increase in temperature decreases the ridge height because of an increase in stress. The widths of ridges increase with increases in strain and temperature.

Vertically stacked vdW multilayers show interesting effects from compressive and uniaxial stretching.³⁶ Figure 2 shows the results of the vdW interaction between a pristine MoSe₂ monolayer placed beneath another monolayer that is under a biaxial compressive strain of 6%. The strained top monolayer has Miura folds like those in Figure 1b. The inhomogeneous stresses in the strained top layer induce a Miura-Ori pattern in the pristine layer, as well. Figure 2a shows out-of-plane deformation, z , in the bilayer at 200 K. The deformations range from -30 Å (dark blue) to 130 Å (brown). Large deformations in red-brown regions are separated by valleys (blue), and they occur along narrow wavy lines (green) in which the displacements along z are small. Figure 2b shows atomic stresses on Mo atoms in the bilayer at 200 K. The stresses are small at the peaks and valleys of out-of-plane deformations, but they are much larger along the green wavy lines of Figure 2a. The CNN analysis reveals the presence of the 2H (dark blue) and 1T (light blue) phases and defects (green) (see Figure 2c). The 2H phase is in low-stress regions, and the 1T phase is in higher-stress regions. Line defects α and β as well as point defects are found in regions of high compressive stress. Panels d–f of Figure 2 show that the system is predominantly in the 2H phase with small fractions of the 1T phase and defects. The

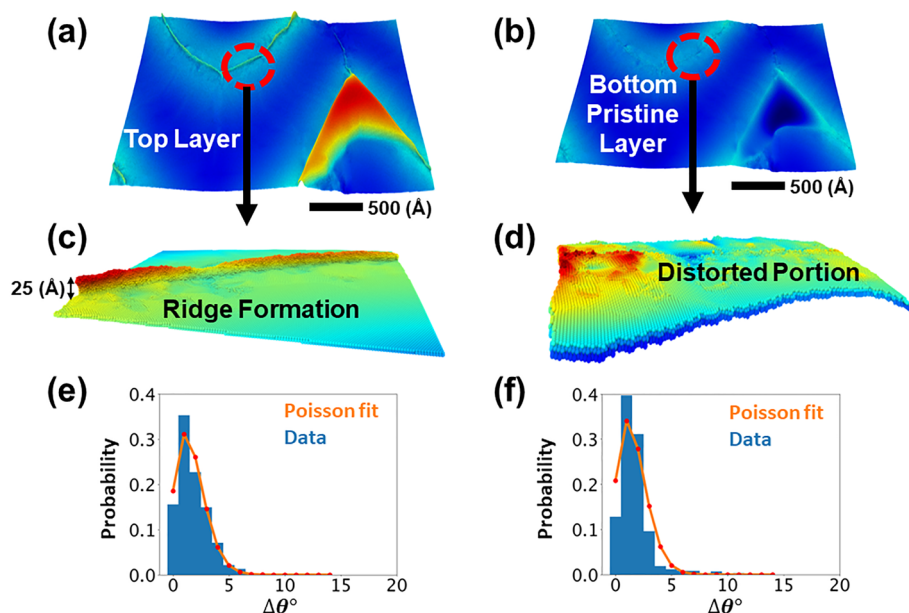


Figure 4. Effect of vdw interaction on Miura folds in individual monolayers of a bilayer system under a 6% compressive strain in both x and y directions. Panels a and b show a small region of a Miura fold in the bottom and top monolayers. Close-ups of that region in panels c and d, respectively, reveal a tiny wrinkle in the bottom layer that distorts the region right above it in the top monolayer. Selenium layers in the tiny wrinkle and the distorted region have twisted relative to each other. The twist angles are narrowly distributed around 2° . The Poisson distributions for the two layers are given in panels e and f, respectively.

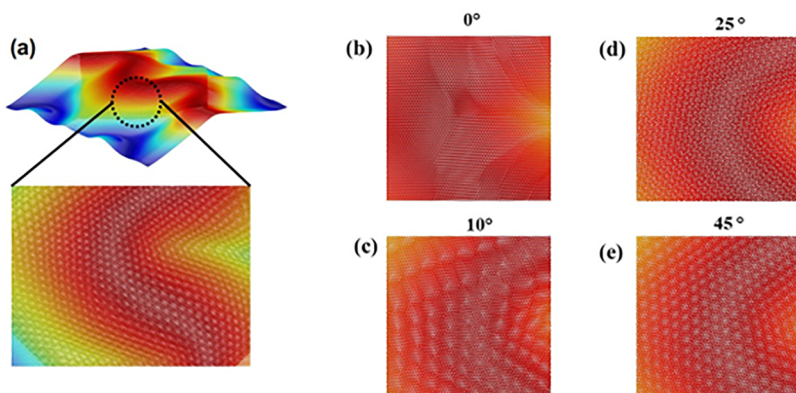


Figure 5. Changes in moiré patterns with the twist angle in a bilayer under a biaxial strain of 6%. Panel a indicates a close-up of a Miura fold we have examined as the top monolayer is rotated relative to the bottom layer. (b) At 0° , there is no moiré pattern. Formation of a hexagonal supercell is observed with an increase in twist angle rotation. Panel c shows hexagonal cells at 10° . (d) The size of these cells decreases upon further rotation. (e) Beyond 30° the hexagonal cells increase in size again.

fractions of 2H and 1T phases decrease almost linearly above 150 K, while defects increase linearly with an increase in temperature.

We have examined the underlying potential energy surfaces (PES) of strained bilayers at various temperatures between 50 and 300 K. The PES were obtained by subjecting atomic configurations to steepest descent quench (SDQ) at regular time intervals of the MD trajectory. A SDQ brings the bilayers to the closest underlying potential energy minimum by removing the kinetic energy. Figure 3 shows the PES for a bilayer under biaxial compression, and Figure S6 shows the results under 6% uniaxial compression. Panels a and b of Figure 3 display Miura-Ori patterns at 200 and 300 K, respectively. They do not seem to change very much except that the valleys (blue regions) are slightly shallower at higher temperatures. However, the underlying PES reveals significant differences between the atomic configurations at 200 and 300

K. The PES plots are obtained by generating pixels on an $x-y$ grid of the bilayer and averaging potential energies of atoms in pixels. The potential energies of pixels are plotted along the z axis. The dark brown regions in the Miura-Ori pattern shown in panels a and b of Figure 3 have higher potential energies, while the ridges adjacent to it have lower potential energies. The PES show deep drops in the blue wavy patterns corresponding to the valleys of Miura-Ori patterns. The decrease in potential energy is larger at higher temperatures.

In flat regions of bilayers, the two MoSe₂ sheets are not in complete registry. They contain tiny wrinkles and interesting moiré patterns that arise from a small relative rotation between Se layers. The moiré patterns are different in the bilayers because the relative rotations of Se layers are different under uniaxial and biaxial compressions. The rotation is $<2^\circ$ for bilayers subjected to uniaxial compression and slightly larger for bilayers under biaxial compression. We also find tiny

wrinkles in flat portions of bilayers. Figure 4a shows a small flat region of the top monolayer that was subjected to 6% biaxial compression. The close-up in Figure 4c reveals tiny wrinkles with heights of $<5\text{ \AA}$. A tiny wrinkle also appears in the bottom layer (see panels b and d of Figure 4). The twist angle distributions shown in panels e and f of Figure 4 are similar for wrinkles in the top and bottom layers. Both are Poisson distributions with peaks around 2° . Similar types of minuscule wrinkles were seen in graphene bilayers using a superconducting quantum interference device.³⁷

We have examined moiré patterns in strained MoSe₂ bilayers subjected to relative twist between the monolayers. The top MoSe₂ monolayer was rotated relative to the bottom monolayer, and then the bilayers were relaxed by the conjugate minimization method and thermalized at different temperatures. Here we present the results for a biaxially strained system at 200 K. The system size is $800\text{ \AA} \times 400\text{ \AA}$, and the applied strain is 1%. Figure 5a shows a Miura-Ori pattern in one of the MoSe₂ monolayers, and the close-up indicates the region in which we have examined the changes in moiré patterns with the angle of rotation. The peaks and valleys in the pattern range from -3 to 3 \AA . The CNN analysis reveals a strained 2H structure in the Miura folds. Figure 5b shows the moiré pattern before twisting, and panels c–e of Figure 5 show how twisting changes those patterns. Upon twisting, larger moiré patterns appear periodically followed by smaller ones. Figure 5c shows large hexagons in the moiré pattern at a twist angle of 10° . The size of hexagons is very sensitive to the twist angle. A further increase in the twist angle first decreases and then increases the size of hexagons in moiré patterns. Panels d and e of Figure 5 show restoration of large moiré patterns at twist angles of 25° and 45° , respectively.

In summary, 2D MoSe₂ displays interesting structural transformations under compressive strains. In monolayers, periodic wrinkles are formed under uniaxial strain and Miura-Ori patterns under biaxial strain. When a pristine MoSe₂ layer is vertically stacked on a uniaxially strained monolayer, the vdW interaction induces wrinkle–ridge transformation in the resulting bilayer. Biaxial strain induces commensurate and incommensurate Miura-Ori patterns in MoSe₂ bilayers. Wrinkles, ridges, and Miura folds consist of a strained semiconducting 2H phase in which the atomic layers of Se are slightly twisted relative to each other. Twist angles are randomly distributed with peaks around 2° . In addition to the predominant 2H phase, there are small islands of the metallic 1T phase and chain-like defects in high-stress regions of wrinkles, ridges, and Miura folds. Relative rotation between the monolayers produces interesting changes in moiré patterns that are periodic functions of the twist angle.

Wrinkles, ridges, and Miura-Ori patterns can be tuned by uniaxial and biaxial strains, and in turn, they can dramatically change the electronic and optoelectronic properties of 2D materials.^{38–41} Defects present in TMDCs also impact their electronic properties.⁴² Vertical stacking and the varying composition of TMDCs with other 2D materials like graphene and hBN can tune the bandgap and exciton binding energy of these materials.^{43,44} Castellanos-Gomez et al. have examined the effect of wrinkles on optoelectronic properties through local strain engineering of atomically thin MoS₂ supported on elastomeric substrates.⁴⁵ They observe a red shift in the photoluminescence signal from a wrinkled MoS₂ sheet relative to the signal from a flat monolayer, which indicates a reduction in the bandgap due to strains in the wrinkled sheet.

Furthermore, they observe excitons drifting from high-stress slopes to low-stress regions on the wrinkle peaks. Through strain engineering of 2D TMDCs, it is possible to generate interesting hybrid metasurfaces consisting of metallic 1T and semiconducting 2H phases with variable bandgaps. Vertically stacked TMDCs with hybrid metallic and semiconducting metasurfaces offer exciting possibilities for nanophotonics applications.

■ COMPUTATIONAL METHODS

The force field for the simulations was developed with a data set generated by density functional theory simulations, and the parameters in two- and three-body interactions were fitted to structural and mechanical properties and vibrational densities of states of unstrained and strained MoSe₂.^{46,47} The force field was validated against quantum dynamics simulation and experimental data. Details of the force field development and validation are provided in the Supporting Information.

After validation, we performed MD simulations on unstrained MoSe₂ monolayers with dimensions of $400\text{ \AA} \times 200\text{ \AA}$, $800\text{ \AA} \times 400\text{ \AA}$, $1000\text{ \AA} \times 1000\text{ \AA}$, $1600\text{ \AA} \times 800\text{ \AA}$, and $3200\text{ \AA} \times 1600\text{ \AA}$. These systems were relaxed using the conjugate gradient minimization scheme and then strained incrementally. Uniaxial compression transforms flat sheets into wrinkled sheets, and biaxial compression generates Miura-Ori patterns in monolayers (see Figure S3). The unstrained and strained MoSe₂ sheets were heated to various temperatures and thermalized for 1 ns in the NVT ensemble, and the properties and processes in equilibrated systems were examined over 0.5 ns.

Bilayer systems were created by placing strained layers over pristine MoSe₂ monolayers and then relaxed with the conjugate gradient minimization scheme. The bilayers were heated and thermalized in the NVT ensemble, and the structural, mechanical, and dynamical properties of thermalized bilayers were computed in the NVE ensemble.

Analysis Using Convolutional Neural Networks. Classification of crystalline phases (2H and 1T) and defects in strain-induced wrinkles, ridges, and Miura-Ori patterns in MoSe₂ monolayers and bilayers is computationally expensive, especially for large systems consisting of millions of atoms. We address this challenge with a CNN, which is highly efficient and accurate in capturing the complexities of phase transformations and defect distributions in MoSe₂ monolayers and bilayers.^{48,49}

The CNN was trained by converting atomic coordinates to image-based data. The input data consist of $14\text{ \AA} \times 14\text{ \AA}$ patches centered around every Mo atom. These patches are converted into $64 \times 64 \times 3$ tensors using a $0.3\text{ \AA} \times 0.3\text{ \AA}$ grid. Channels 1 and 3 of the input tensors correspond to the top and bottom Se layers, respectively, and channel 2 corresponds to the middle Mo layer. The atomic coordinates are transformed into a tensor using an exponential kernel

$$T_{c=1,2,3}(x, y) = \sum_{i=1}^N \exp \left[-\frac{(x - x_i)^2 + (y - y_i)^2}{\eta^2} \right] \quad (1)$$

where c refers to the input channel, (x, y) corresponds to the center of a grid, (x_i, y_i) are the coordinates of Mo and Se atoms, and N is the total number of atoms within a $14\text{ \AA} \times 14\text{ \AA}$ patch around the central Mo atom. The width of the exponential kernel η is set to 0.2 \AA .

The CNN architecture is shown in Figure S3. It consists of three convolutional layers with dimensions of $32 \times 32 \times 32$, 64

$\times 16 \times 16$, and $64 \times 8 \times 8$ and two fully connected layers with 4096 and 10 units. A softmax layer at the end outputs a number corresponding to 2H, 1T, and various defects. The stride size in each convolutional layer is 1, and the filter size is 3; we use a leakyReLU activation function ($\alpha = 0.2$).

Transfer Learning. The CNN was trained on data from the simulation trajectory of crack propagation in a MoWSe₂ alloy.^{33,50,51} The neural network could accurately identify not only 2H and 1T phases but also point and extended defects at 2H–1T interfaces in the alloy. The CNN trained with crack propagation data in MoWSe₂ under tensile strain is used to analyze local structural changes induced by lateral compression in monolayer and bilayer MoSe₂. The set of training data contains 40 000 simulation images of MoWSe₂ under tensile strain and only 1000 images from the data set on MoSe₂ monolayers. To validate CNN transfer learning, the trained neural network is tested on the remaining data sets of laterally compressed MoSe₂ monolayers and bilayers. It correctly classifies atoms in 2H and 1T phases and chain-like defects that have been seen in STEM images of MoS₂.³⁵ The accuracy of the CNN on the test data sets is 97% (see Figure S3).

ASSOCIATED CONTENT

Supporting Information

The Supporting Information is available free of charge at <https://pubs.acs.org/doi/10.1021/acs.jpcllett.2c03539>.

Force field parametrization and validation (Figure S1), convolutional neural network architecture and validation (Figure S2), structure and stress distribution in a uniaxially strained MoSe₂ monolayer (Figure S3), wrinkle–ridge transformation in a MoSe₂ bilayer (Figure S4), effect of strain on ridge formation in a MoSe₂ bilayer (Figure S5), and energetics of ridges in MoSe₂ bilayers (Figure S6) ([PDF](#))

Biaxial compression of MoSe₂ and emergence of Miura-Ori patterns ([MP4](#))

Biaxial compression of MoSe₂ and emergence of 2H and 1T phases ([MP4](#))

AUTHOR INFORMATION

Corresponding Author

Rajiv K. Kalia – Collaboratory for Advanced Computing and Simulations, Department of Chemical Engineering and Materials Science, Department of Physics & Astronomy, and Department of Computer Science, University of Southern California, Los Angeles, California 90089, United States; Phone: (213) 821-2658; Email: rkalia@usc.edu; Fax: (213)-821-2664

Authors

Anikeya Aditya – Collaboratory for Advanced Computing and Simulations, Department of Chemical Engineering and Materials Science, Department of Physics & Astronomy, and Department of Computer Science, University of Southern California, Los Angeles, California 90089, United States; [orcid.org/0000-0001-9533-7666](#)

Ankit Mishra – Collaboratory for Advanced Computing and Simulations, Department of Chemical Engineering and Materials Science, Department of Physics & Astronomy, and Department of Computer Science, University of Southern California, Los Angeles, California 90089, United States; [orcid.org/0000-0002-3372-4684](#)

Nitish Baradwaj – Collaboratory for Advanced Computing and Simulations, Department of Chemical Engineering and Materials Science, Department of Physics & Astronomy, and Department of Computer Science, University of Southern California, Los Angeles, California 90089, United States

Ken-ichi Nomura – Collaboratory for Advanced Computing and Simulations, Department of Chemical Engineering and Materials Science, Department of Physics & Astronomy, and Department of Computer Science, University of Southern California, Los Angeles, California 90089, United States

Aiichiro Nakano – Collaboratory for Advanced Computing and Simulations, Department of Chemical Engineering and Materials Science, Department of Physics & Astronomy, and Department of Computer Science, University of Southern California, Los Angeles, California 90089, United States; [orcid.org/0000-0003-3228-3896](#)

Priya Vashishta – Collaboratory for Advanced Computing and Simulations, Department of Chemical Engineering and Materials Science, Department of Physics & Astronomy, and Department of Computer Science, University of Southern California, Los Angeles, California 90089, United States; [orcid.org/0000-0003-4683-429X](#)

Complete contact information is available at:

<https://pubs.acs.org/10.1021/acs.jpcllett.2c03539>

Notes

The authors declare no competing financial interest.

ACKNOWLEDGMENTS

This work was supported by the National Science Foundation, Future Manufacturing Program, via Grant 2036359 and performed, in part, at the Center for Integrated Nanotechnologies, an Office of Science User Facility operated for the U.S. Department of Energy Office (DOE) of Science. Sandia National Laboratories is a multimission laboratory managed and operated by National Technology & Engineering Solutions of Sandia, LLC, a wholly owned subsidiary of Honeywell International, Inc., for the U.S. DOE's National Nuclear Security Administration under Contract DE-NA-0003525. The authors thank Dr. Pankaj Rajak, Amazon Research, for helping us with the CNN analysis.

REFERENCES

- (1) Xu, W.; Gracias, D. H. Soft Three-Dimensional Robots with Hard Two-Dimensional Materials. *ACS Nano* **2019**, *13*, 4883–4892.
- (2) Blees, M. K.; Barnard, A. W.; Rose, P. A.; Roberts, S. P.; McGill, K. L.; Huang, P. Y.; Ruyack, A. R.; Kevek, J. W.; Kobrin, B.; Muller, D. A.; McEuen, P. L. Graphene Kirigami. *Nature* **2015**, *524* (7564), 204–207.
- (3) Cai, L.; Shearer, M. J.; Zhao, Y.; Hu, Z.; Wang, F.; Zhang, Y.; Eliceiri, K. W.; Hamers, R. J.; Yan, W.; Wei, S.; Tang, M.; Jin, S. Chemically Derived Kirigami of WSe₂. *J. Am. Chem. Soc.* **2018**, *140* (35), 10980–10987.
- (4) Wang, B.; Nakano, A.; Vashishta, P. D.; Kalia, R. K. Nanoindentation on Monolayer MoS₂ Kirigami. *ACS Omega* **2019**, *4* (6), 9952–9956.
- (5) Zhao, H.; Wang, B.; Liu, F.; Yan, X.; Wang, H.; Leong, W. S.; Stevens, M. J.; Vashishta, P.; Nakano, A.; Kong, J.; Kalia, R.; Wang, H. Fluidic Flow Assisted Deterministic Folding of Van Der Waals Materials. *Adv. Funct. Mater.* **2020**, *30* (13), 1908691.
- (6) Cao, Y.; Fatemi, V.; Fang, S.; Watanabe, K.; Taniguchi, T.; Kaxiras, E.; Jarillo-Herrero, P. Unconventional Superconductivity in Magic-Angle Graphene Superlattices. *Nature* **2018**, *556* (7699), 43–50.

- (7) Carr, S.; Massatt, D.; Fang, S.; Cazeaux, P.; Luskin, M.; Kaxiras, E. Twistrronics: Manipulating the Electronic Properties of Two-Dimensional Layered Structures through Their Twist Angle. *Phys. Rev. B* **2017**, *95* (7), 075420.
- (8) Yu, H.; Liu, G.-B.; Tang, J.; Xu, X.; Yao, W. Moiré Excitons: From Programmable Quantum Emitter Arrays to Spin-Orbit-Coupled Artificial Lattices. *Sci. Adv.* **2017**, *3* (11), 1701696.
- (9) Li, T.; Jiang, S.; Li, L.; Zhang, Y.; Kang, K.; Zhu, J.; Watanabe, K.; Taniguchi, T.; Chowdhury, D.; Fu, L.; Shan, J.; Mak, K. F. Continuous Mott Transition in Semiconductor Moiré Superlattices Electric-Field-Tuned MITs. *Nature* **2021**, *597*, 350.
- (10) Jiang, L.; Shi, Z.; Zeng, B.; Wang, S.; Kang, J.-H.; Joshi, T.; Jin, C.; Ju, L.; Kim, J.; Lyu, T.; Shen, Y.-R.; Crommie, M.; Gao, H.-J.; Wang, F. Soliton-Dependent Plasmon Reflection at Bilayer Graphene Domain Walls. *Nat. Mater.* **2016**, *15* (8), 840–844.
- (11) Sunku, S. S.; Ni, G. X.; Jiang, B. Y.; Yoo, H.; Sternbach, A.; McLeod, A. S.; Stauber, T.; Xiong, L.; Taniguchi, T.; Watanabe, K.; Kim, P.; Fogler, M. M.; Basov, D. N. Photonic Crystals for Nano-Light in Moiré Graphene Superlattices. *Science* **2018**, *362* (6419), 1153–1156.
- (12) Tran, K.; Moody, G.; Wu, F.; Lu, X.; Choi, J.; Kim, K.; Rai, A.; Sanchez, D. A.; Quan, J.; Singh, A.; Embley, J.; Zepeda, A.; Campbell, M.; Autry, T.; Taniguchi, T.; Watanabe, K.; Lu, N.; Banerjee, S. K.; Silverman, K. L.; Kim, S.; Tutuc, E.; Yang, L.; MacDonald, A. H.; Li, X. Evidence for Moiré Excitons in van Der Waals Heterostructures. *Nature* **2019**, *567* (7746), 71–75.
- (13) Seyler, K. L.; Rivera, P.; Yu, H.; Wilson, N. P.; Ray, E. L.; Mandrus, D. G.; Yan, J.; Yao, W.; Xu, X. Signatures of Moiré-Trapped Valley Excitons in MoSe₂/WSe₂ Heterobilayers. *Nature* **2019**, *567* (7746), 66–70.
- (14) Jin, C.; Regan, E. C.; Yan, A.; Iqbal Bakti Utama, M.; Wang, D.; Zhao, S.; Qin, Y.; Yang, S.; Zheng, Z.; Shi, S.; Watanabe, K.; Taniguchi, T.; Tongay, S.; Zettl, A.; Wang, F. Observation of Moiré Excitons in WSe₂/WS₂ Heterostructure Superlattices. *Nature* **2019**, *567* (7746), 76–80.
- (15) Alexeev, E. M.; Ruiz-Tijerina, D. A.; Danovich, M.; Hamer, M. J.; Terry, D. J.; Nayak, P. K.; Ahn, S.; Pak, S.; Lee, J.; Sohn, J. I.; Molas, M. R.; Koperski, M.; Watanabe, K.; Taniguchi, T.; Novoselov, K. S.; Gorbachev, R. v.; Shin, H. S.; Fal'ko, V. I.; Tartakovskii, A. I. Resonantly Hybridized Excitons in Moiré Superlattices in van Der Waals Heterostructures. *Nature* **2019**, *567* (7746), 81–86.
- (16) Wu, F.; Lovorn, T.; Macdonald, A. H. Topological Exciton Bands in Moiré Heterojunctions. *Phys. Rev. Lett.* **2017**, *118* (14), 147401.
- (17) Manchanda, P.; Kumar, P.; Dev, P. Thickness Dependence of Hydrogen-Induced Phase Transition in MoTe₂. *Phys. Rev. B* **2020**, *101* (14), 144104.
- (18) Lee, K.; Hazra, T.; Randeria, M.; Trivedi, N. Topological Superconductivity in Dirac Honeycomb Systems. *Phys. Rev. B* **2019**, *99* (18), 184514.
- (19) Jin, L.; Takei, A.; Hutchinson, J. W. Mechanics of Wrinkle/Ridge Transitions in Thin Film/Substrate Systems. *J. Mech. Phys. Solids* **2015**, *81*, 22–40.
- (20) Mahadevan, L.; Rica, S. Self-Organized Origami. *Science* **2005**, *307* (5716), 1740.
- (21) Bowden, N.; Brittain, S.; Evans, A. G.; Hutchinson, J. W.; Whitesides, G. M. Spontaneous Formation of Ordered Structures in Thin Films of Metals Supported on an Elastomeric Polymer. *Nature* **1998**, *393* (6681), 146.
- (22) Yu, H.; Liu, G.-B.; Tang, J.; Xu, X.; Yao, W. Moiré Excitons: From Programmable Quantum Emitter Arrays to Spin-Orbit-Coupled Artificial Lattices. *Sci. Adv.* **2017**, *3* (11), 1701696.
- (23) Brau, F.; Vandeparre, H.; Sabbah, A.; Poulard, C.; Boudaoud, A.; Damman, P. Multiple-Length-Scale Elastic Instability Mimics Parametric Resonance of Nonlinear Oscillators. *Nat. Phys.* **2011**, *7* (1), 56–60.
- (24) Brau, F.; Damman, P.; Diamant, H.; Witten, T. A. Wrinkle to Fold Transition: Influence of the Substrate Response. *Soft Matter* **2013**, *9* (34), 8177–8186.
- (25) Holmes, D. P.; Crosby, A. J. Draping Films: A Wrinkle to Fold Transition. *Phys. Rev. Lett.* **2010**, *105* (3), 038303.
- (26) Kim, P.; Abkarian, M.; Stone, H. A. Hierarchical Folding of Elastic Membranes under Biaxial Compressive Stress. *Nat. Mater.* **2011**, *10* (12), 952–957.
- (27) Pocivavsek, L.; Dellsy, R.; Kern, A.; Johnson, S.; Lin, B.; Lee, K. Y. C.; Cerdá, E. Stress and Fold Localization in Thin Elastic Membranes. *Science* **2008**, *320* (5878), 912–916.
- (28) Sun, J. Y.; Xia, S.; Moon, M. W.; Oh, K. H.; Kim, K. S. Folding Wrinkles of a Thin Stiff Layer on a Soft Substrate. *Proc. R. Soc. A* **2012**, *468*, 932–953.
- (29) Jahan Sajib, M. S.; Wei, Y.; Mishra, A.; Zhang, L.; Nomura, K.-I.; Kalia, R. K.; Vashishta, P.; Nakano, A.; Murad, S.; Wei, T. Atomistic Simulations of Biofouling and Molecular Transfer of a Cross-Linked Aromatic Polyamide Membrane for Desalination. *Langmuir* **2020**, *36* (26), 7658–7668.
- (30) Tiwari, S. C.; Shimamura, K.; Mishra, A.; Shimojo, F.; Nakano, A.; Kalia, R. K.; Vashishta, P.; Branicio, P. S. Hydrogen Bond Preserving Stress Release Mechanism Is Key to the Resilience of Aramid Fibers. *J. Phys. Chem. B* **2019**, *123* (45), 9719–9723.
- (31) Mishra, A.; Krishnamoorthy, A.; Rajak, P.; Tiwari, S.; Sheng, C.; Kalia, R. K.; Nakano, A.; Vashishta, P. Free Energy of Hydration and Heat Capacity of Calcium Dipicolinate in Bacillus Spore Cores. *Appl. Phys. Lett.* **2018**, *113* (11), 113702.
- (32) Rajak, P.; Mishra, A.; Sheng, C.; Tiwari, S.; Krishnamoorthy, A.; Kalia, R. K.; Nakano, A.; Vashishta, P. Gel Phase in Hydrated Calcium Dipicolinate. *Appl. Phys. Lett.* **2017**, *111* (21), 213701.
- (33) Rajak, P.; Krishnamoorthy, A.; Nakano, A.; Vashishta, P.; Kalia, R. Structural Phase Transitions in a MoWSe₂ Monolayer: Molecular Dynamics Simulations and Variational Autoencoder Analysis. *Phys. Rev. B* **2019**, *100* (1), 014108.
- (34) Krishnamoorthy, A.; Nomura, K.; Baradwaj, N.; Shimamura, K.; Rajak, P.; Mishra, A.; Fukushima, S.; Shimojo, F.; Kalia, R.; Nakano, A.; Vashishta, P. Dielectric Constant of Liquid Water Determined with Neural Network Quantum Molecular Dynamics. *Phys. Rev. Lett.* **2021**, *126* (21), 216403.
- (35) Lin, Y. C.; Dumcenco, D. O.; Huang, Y. S.; Suenaga, K. Atomic Mechanism of the Semiconducting-to-Metallic Phase Transition in Single-Layered MoS₂. *Nat. Nanotechnol.* **2014**, *9* (5), 391–396.
- (36) Huang, Z.; Cuniberto, E.; Park, S.; Kisslinger, K.; Wu, Q.; Taniguchi, T.; Watanabe, K.; Yager, K. G.; Shahrjerdi, D. Mechanisms of Interface Cleaning in Heterostructures Made from Polymer-Contaminated Graphene. *Small* **2022**, *18* (20), 2201248.
- (37) Uri, A.; Grover, S.; Cao, Y.; Crosse, J. A.; Bagani, K.; Rodan-Legrain, D.; Myasoedov, Y.; Watanabe, K.; Taniguchi, T.; Moon, P.; Koshino, M.; Jarillo-Herrero, P.; Zeldov, E. Mapping the Twist-Angle Disorder and Landau Levels in Magic-Angle Graphene. *Nature* **2020**, *581* (7806), 47–52.
- (38) Zhang, K.; Guo, Y.; Larson, D. T.; Zhu, Z.; Fang, S.; Kaxiras, E.; Kong, J.; Huang, S. Spectroscopic Signatures of Interlayer Coupling in Janus MoSSe/MoS₂ Heterostructures. *ACS Nano* **2021**, *15* (9), 14394–14403.
- (39) Defo, R. K.; Fang, S.; Shirodkar, S. N.; Tritsaris, G. A.; Dimoulas, A.; Kaxiras, E. Strain Dependence of Band Gaps and Exciton Energies in Pure and Mixed Transition-Metal Dichalcogenides. *Phys. Rev. B* **2016**, *94* (15), 155310.
- (40) Yang, J.; Colen, J.; Liu, J.; Nguyen, M. C.; Chern, G.; Louca, D. Elastic and Electronic Tuning of Magnetoresistance in MoTe₂. *Sci. Adv.* **2017**, *3* (12), aao4949.
- (41) Li, H.; Contryman, A. W.; Qian, X.; Ardakani, S. M.; Gong, Y.; Wang, X.; Weisse, J. M.; Lee, C. H.; Zhao, J.; Ajayan, P. M.; Li, J.; Manoharan, H. C.; Zheng, X. Optoelectronic Crystal of Artificial Atoms in Strain-Textured Molybdenum Disulfide. *Nat. Commun.* **2015**, *6* (1), 7381.
- (42) Chen, Y.; Huang, S.; Ji, X.; Adeppali, K.; Yin, K.; Ling, X.; Wang, X.; Xue, J.; Dresselhaus, M.; Kong, J.; Yildiz, B. Tuning Electronic Structure of Single Layer MoS₂ through Defect and Interface Engineering. *ACS Nano* **2018**, *12* (3), 2569–2579.

- (43) Raja, A.; Chaves, A.; Yu, J.; Arefe, G.; Hill, H. M.; Rigosi, A. F.; Berkelbach, T. C.; Nagler, P.; Schüller, C.; Korn, T.; Nuckolls, C.; Hone, J.; Brus, L. E.; Heinz, T. F.; Reichman, D. R.; Chernikov, A. Coulomb Engineering of the Bandgap and Excitons in Two-Dimensional Materials. *Nat. Commun.* **2017**, *8* (1), 15251.
- (44) Mann, J.; Ma, Q.; Odenthal, P. M.; Isarraraz, M.; Le, D.; Preciado, E.; Barroso, D.; Yamaguchi, K.; von Son Palacio, G.; Nguyen, A.; Tran, T.; Wurch, M.; Nguyen, A.; Klee, V.; Bobek, S.; Sun, D.; Heinz, T. F.; Rahman, T. S.; Kawakami, R.; Bartels, L. 2-Dimensional Transition Metal Dichalcogenides with Tunable Direct Band Gaps: $\text{MoS}_{2(1-x)}\text{Se}_{2x}$ Monolayers. *Adv. Mater.* **2014**, *26* (9), 1399–1404.
- (45) Castellanos-Gomez, A.; Roldán, R.; Cappelluti, E.; Buscema, M.; Guinea, F.; van der Zant, H. S. J.; Steele, G. A. Local Strain Engineering in Atomically Thin MoS₂. *Nano Lett.* **2013**, *13* (11), 5361–5366.
- (46) Krishnamoorthy, A.; Mishra, A.; Grabar, N.; Baradwaj, N.; Kalia, R.; Nakano, A.; Vashishta, P. Evolutionary Multi-Objective Optimization and Pareto-Frontal Uncertainty Quantification of Interatomic Forcefields for Thermal Conductivity Simulations. *Comput. Phys. Commun.* **2020**, *254*, 107337.
- (47) Mishra, A.; Hong, S.; Rajak, P.; Sheng, C.; Nomura, K.; Kalia, R. K.; Nakano, A.; Vashishta, P. Multiobjective Genetic Training and Uncertainty Quantification of Reactive Force Fields. *npj Comput. Mater.* **2018**, *4* (1), 42.
- (48) Nazarova, A. L.; Yang, L.; Liu, K.; Mishra, A.; Kalia, R. K.; Nomura, K.; Nakano, A.; Vashishta, P.; Rajak, P. Dielectric Polymer Property Prediction Using Recurrent Neural Networks with Optimizations. *J. Chem. Inf. Model.* **2021**, *61* (5), 2175–2186.
- (49) Rajak, P.; Krishnamoorthy, A.; Mishra, A.; Kalia, R.; Nakano, A.; Vashishta, P. Autonomous Reinforcement Learning Agent for Chemical Vapor Deposition Synthesis of Quantum Materials. *npj Comput. Mater.* **2021**, *7* (1), 108.
- (50) Krizhevsky, A.; Sutskever, I.; Hinton, G. E. ImageNet Classification with Deep Convolutional Neural Networks. In *Advances in Neural Information Processing Systems*; Pereira, F., Burges, C. J., Bottou, L., Weinberger, K. Q., Eds.; Curran Associates, Inc., 2012; Vol. 25.
- (51) Stillinger, F. H.; Weber, T. A. Computer Simulation of Local Order in Condensed Phases of Silicon. *Phys. Rev. B* **1985**, *31* (8), 5262–5271.

□ Recommended by ACS

Revealing 3D Ripple Structure and Its Dynamics in Freestanding Monolayer MoSe₂ by Single-Frame 2D Atomic Image Reconstruction

Songge Li, Junhao Lin, *et al.*

FEBRUARY 13, 2023

NANO LETTERS

READ ▶

Surface-Dependent Adhesion Properties of Graphene on Diamonds for the Fabrication of Nanodevices: A Molecular Dynamics Investigation

Shandeng Chen, Yuhao Dou, *et al.*

FEBRUARY 08, 2023

ACS APPLIED NANO MATERIALS

READ ▶

Electron-Beam- and Thermal-Annealing-Induced Structural Transformations in Few-Layer MnPS₃

Alexander Storm, Ute Kaiser, *et al.*

FEBRUARY 20, 2023

ACS NANO

READ ▶

Chirality Dependence of Triplet Excitons in (6,5) and (7,5) Single-Wall Carbon Nanotubes Revealed by Optically Detected Magnetic Resonance

Ivan Sudakov, Sofie Cambré, *et al.*

JANUARY 20, 2023

ACS NANO

READ ▶

Get More Suggestions >